

Acoustic Emissions Monitoring during Inelastic Deformation of Porous Sandstone: Comparison of Three Modes of Deformation

JEROME FORTIN,¹ SERGEI STANCHITS,² GEORG DRESEN,² and YVES GUEGUEN¹

Abstract—In some reservoirs, large deformations can occur during oil or gas production because of the effective stress change. For very porous rocks, these production operations can be sufficient to cause inelastic deformation and irreversible damage. Rock formations can undergo deformation by different mechanisms, including dilatancy or pore collapse. In the laboratory, it has been shown that the inelastic deformation and failure mode of porous rocks are pressure sensitive. Indeed, when subjected to an overall compressive loading, a porous rock may fail by shear localization, compaction localization, or by cataclastic compaction. Acoustic emission (AE) records provide important information to understand the failure mode of rocks: the spatial evolution of damage as well as the source mechanisms can be followed using this technique. In this paper, we present three different laboratory axisymmetric compression experiments, performed on Bleurswiller sandstone, which enable us to compare the acoustic emission signature of these three modes of deformation. Our data show that compaction localization and cataclastic compaction are characterized by similar acoustic signatures (in terms of AE sources characteristics and evolution of AE number), in comparison to the acoustic signature from shear localization. This implies similar micromechanisms involved during compaction bands formation and cataclastic compaction.

Key words: Porous sandstone, acoustic emissions, source mechanisms, shear localization, compaction bands, cataclastic compaction.

1. Introduction

When subjected to an overall compressive loading, a rock can fail by shear localization, compaction localization or cataclastic compaction (WONG *et al.*, 1997, 2004; KLEIN *et al.*, 2001; FORTIN *et al.*, 2005). The laboratory investigations provide important physical insights into tectonic processes in relation to faulting, in sandstone formation, as well as reservoir and geotechnical problems. Reservoir compaction is one of the most important processes in the oil and gas industry. Hydrocarbon production decreases the pore pressure and hence increases the effective stress. For very porous rock, the changes in effective stresses can be sufficient to induce inelastic deformation, which can i) lead to seafloor

¹ Laboratoire de Géologie, Ecole Normale Supérieure, CNRS, UMR 8538, 24 Rue Lhomond, 75005 Paris, France. E-mail: fortin@geologie.ens.fr

² GeoForschungsZentrum Potsdam, Telegrafenberg, D-14473 Potsdam, Germany.
E-mail: stanch@gfz-potsdam.de

subsidence (for example, the extraction of oil and gas in the Ekofisk field in the North Sea has produced a subsidence of more than 4 meters); ii) cause casing failures; or iii) can decrease significantly the permeability of the reservoir (NAGEL, 2001; OSTERMEIER, 2001).

In porous sandstone, a transition in failure mode from brittle faulting to cataclastic compaction occurs as effective pressure increases. Under a relatively low effective confining pressure the differential stress attains a peak before it undergoes strain softening; the failure of sample occurs by shear localization (WONG *et al.*, 1997). Cataclastic compaction is commonly observed as a response to purely hydrostatic loading: Under pressure, the pore space is initially reduced by elastic deformation and the rock becomes stiffer. However, as the hydrostatic loading increases, the rock reaches a critical point, where it suddenly becomes increasingly more compliant, showing a dramatic increase in compaction (ZHANG *et al.*, 1990; DAVID *et al.*, 1994; MENÉNDEZ *et al.*, 1996; WU *et al.*, 2000). In the transitional regime from brittle faulting to cataclastic compaction, different laboratory studies conducted on porous sandstones show that localization can occur purely by compaction, without shear (formation of compaction bands) (KLEIN *et al.*, 2001; BAUD *et al.*, 2004; FORTIN *et al.*, 2005, 2006). Compaction bands are zones of material which extend subperpendicular to the main compressive stress. From microstructural observations a compaction band appears as a crushed zone of reduced porosity. If the microstructure of the rock outside the band remains largely undeformed, inside the band grains are crushed and the fragments fill up the collapsed pore space (BAUD *et al.*, 2004; FORTIN *et al.*, 2006). In addition, significant reduction of permeability has been reported while a sample undergoes compaction localization, which demonstrates that a compaction band acts as a barrier for fluid flow (VAJDOVA *et al.*, 2004).

The three modes of failure, — shear localization, compaction localization, cataclastic compaction — are very different on the macroscopic scale, however they involve similar micromechanical processes. Indeed, grain-scale microcracking is commonly observed (MENÉNDEZ *et al.*, 1996) and as a consequence these three modes of deformation lead to radiation of acoustic emissions. Acoustic emission (AE) records provide important information to understand the failure mode of rocks: (i) AE activity can be recorded using one piezoelectric transducer, and the number of AE can be related to the inelastic deformation (SCHOLZ 1968; SANO *et al.*, 1981), (ii) Using multiple transducers attached to the surface of a specimen under stress, the spatial origin of the damage can be located. For example, different authors have used this technique in axisymmetric compression experiments to investigate shear-fracture nucleation (e.g., LEI, 1992; LOCKNER, 1993; ZANG *et al.*, 1998) and recently to analyze the development of discrete compaction bands (FORTIN *et al.*, 2006; STANCHITS *et al.*, this issue). (iii) Finally AE waveforms provide information on the source mechanisms taking place during the deformation of the rock, allowing a better understanding of the micromechanisms (STANCHITS *et al.*, 2001).

The aim of this study is to focus on the acoustic emission signature of the three modes of failure commonly observed in porous sandstone. In a recent paper, FORTIN *et al.* (2006) used acoustic emission analysis to investigate the formation of compaction bands in Bleurswiller sandstone. Two more experiments have been conducted on this sandstone:

A purely hydrostatic one, and a triaxial compression test at an effective confining pressure of 10 MPa, where shear localization is observed. We also used the data from a triaxial experiment at an effective confining pressure of 70 MPa, published in FORTIN *et al.* (2006), where compaction bands are observed. These three experiments enable us to compare the acoustic emission signature for the three different modes of failure: shear localization, compaction localization and cataclastic compaction.

2. Experimental Procedures

The Bleurswiller sandstone has a nominal porosity of $25\% \pm 0.5\%$. Grain sizes range from $80\ \mu\text{m}$ to $150\ \mu\text{m}$ with a mean value of $110\ \mu\text{m}$. Cylindrical specimens of 100 mm in length and 50 mm in diameter were prepared from the same block as that studied by FORTIN *et al.* (2005, 2006, 2007) and TEMBE *et al.* (2008). As in previous studies, the samples were cored perpendicular to the bedding. Figure 1a) gives a picture of an intact specimen. The modal composition of this sandstone is 50% quartz, 30% feldspars, and 20% oxydes-micas (FORTIN *et al.*, 2006). Fig. 1b) shows a SEM (scanning electron microscopy) of an intact specimen, for comparison: Porosity appears in black and quartz grains appear darker than the feldspar grains.

The experiments were performed at the GeoForschungsZentrum Potsdam. We used a servo-controlled MTS loading frame with load capacity of 4600kN (Fig. 2a). All experiments were carried out at room temperature. Following the methodology of FORTIN *et al.* (2006), the samples were saturated with distilled water and deformed under fully

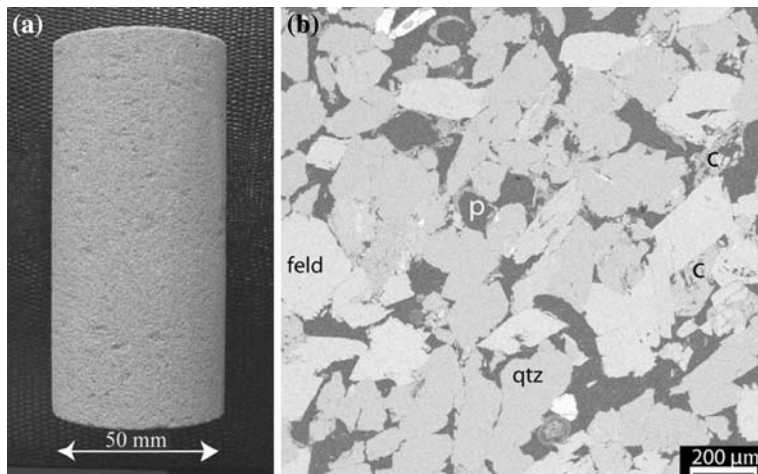


Figure 1

a) Picture of a non-deformed sample of Bleurswiller sandstone. b) SEM micrograph (backscattered) of intact sandstone. Epoxy-filled pores (p) appear in black, porosity is about 25%. Quartz, feldspar, and clay are denoted by qtz, feld, and c, respectively.

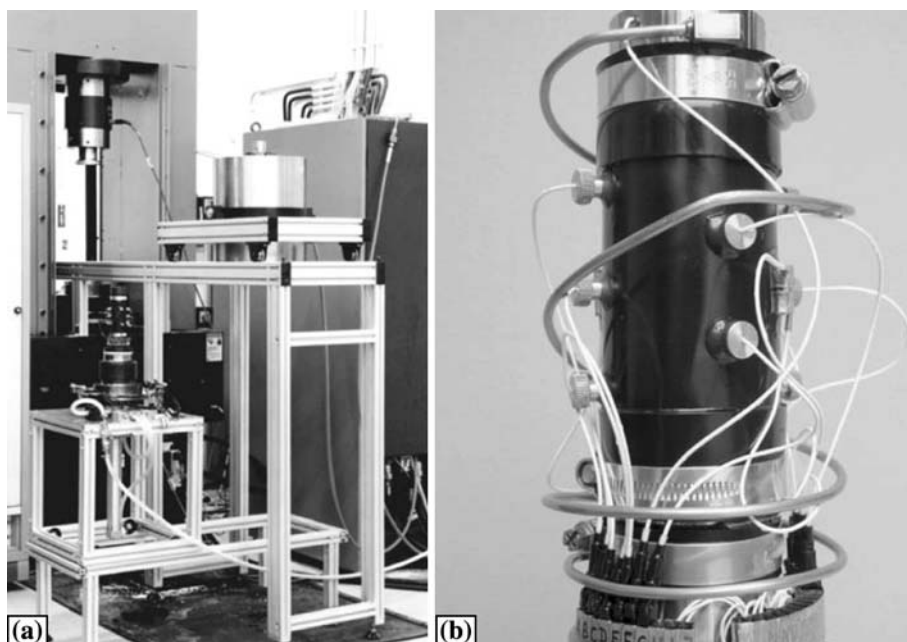


Figure 2

Experimental setup. a) MTS loading frame with 200 MPa pressure vessel. b) Cylindrical specimen encapsulated in rubber jacket with P sensors glued directly on the sample surface.

drained conditions at a constant pore pressure of 10 MPa. The pore pressure was maintained constant, and the variation of pore volume was recorded using a volumeter. From this, the evolution of connected sample porosity was deduced. For the hydrostatic experiment (VO#5), confining pressure was increased up to 120 MPa with a pressurization ramp of 1 MPa/s, then confining pressure was increased by steps of 5 MPa. At the end of each step, confining pressure was kept constant in order to reach equilibrium in pore volume variation. The two triaxial experiments (VO#3 and VO#4) were carried out at a constant strain rate of 10^{-5} s^{-1} .

Then, the deformed samples were unloaded and retrieved from the pressure vessel, the jackets were carefully removed, and samples were impregnated with epoxy for microstructural analysis.

AE activity and elastic wave velocity changes were monitored by twelve *P*-wave piezoelectric sensors, either embedded in the pistons or glued to the sample surface and sealed in a neoprene jacket using two-component epoxy (Fig. 2b). *P*-wave sensors were produced from PZT piezoceramic discs with 5 mm diameter and 2 mm thickness. Transducer signals were amplified by 40 dB using Physical Acoustic Corporation preamplifiers. Full-waveform AE data and the ultrasonic signals for *P*-wave velocity measurements were stored in a 12-channel transient recording system (*DaxBox*, *Prökel*, Germany) with an amplitude resolution of 16 bit at 10 MHz sampling rate. For periodic

elastic wave speed measurements, six P sensors were used as senders applying 100 V pulses every ~ 30 seconds during the loading.

Ultrasonic transmissions and AE waveforms were discriminated automatically after the experiments. Onset time of P wave and AE were picked automatically. Hypocenter locations were estimated, using a downhill simplex algorithm considering time-dependent changes of the anisotropic velocity field. AE events with “adjusted amplitude” exceeding 300 mV were selected. Adjusted amplitude is calculated from the maximum amplitude on each channel and for a distance of 10 mm from the AE hypocenter assuming geometrical spreading of elastic waves (LOCKNER *et al.*, 1992; ZANG *et al.*, 1998). AE hypocenter location errors are estimated to be ± 1 mm (STANCHITS *et al.*, 2006). First-motion amplitudes were picked automatically and first-motion polarities were used to discriminate AE sources types in tensile, shear, and collapse events (ZANG *et al.*, 1998).

3. Results

3.1. Mechanical Data and Failure Mode

In this section, data from two new experiments (VO#4 and VO#5) are presented. We also used data from a triaxial experiment (VO#3) performed at an effective confining pressure of 70 MPa, published in FORTIN *et al.* (2006).

We use, in this study, the convention that compressive stresses and compactive strains are positive. The maximum and minimum (compressive) stresses are denoted by σ_1 and σ_3 , respectively. The pore pressure is denoted by P_p , and the difference between the confining pressure ($P_c = \sigma_3 = \sigma_2$) and the pore pressure is referred to as the “effective confining pressure”. The effective mean stress $(\sigma_1 + 2\sigma_3)/3 - P_p$ will be denoted P and the differential stress $\sigma_1 - \sigma_3$ by Q .

From previous studies performed on Bleurswiller sandstone (FORTIN *et al.*, 2005; TEMBE *et al.*, 2008), the brittle faulting regime is observed for effective confining pressure lower than 30 MPa, whereas discrete compaction bands are observed for effective confining pressure higher than 60 MPa. For effective confining pressure in the range of [30–50 MPa], samples of Bleurswiller sandstone develop a hybrid failure involving both discrete compaction bands and shear bands.

Figure 3 summarizes data for the three samples deformed i) under hydrostatic pressure (VO#5), ii) under triaxial loading at an effective confining pressure of 10 MPa (VO#4), iii) and at an effective confining pressure of 70 MPa (VO#3).

Figure 3a) illustrates the hydrostatic compaction behavior. The first part of the loading is representative of elastic deformation. However at the stress state P^* , the sample shows a dramatic reduction in porosity (cataclastic compaction). This inflection point P^* occurs at an effective pressure of 125 MPa. This value is different from the previous results presented in FORTIN *et al.* (2005), who found 135 MPa. This difference can be partially explained by the methodology: in this study we determined P^* using

mechanical and AE data, whereas in FORTIN *et al.* (2005) the authors mostly relied on mechanical data.

The evolution of cumulative AE number registered during this experiment is given in Figure 4a. The critical stress state P^* coincides with a surge in AE activity in agreement with previous studies (ZHANG *et al.*, 1990; BAUD *et al.*, 2004). Due to the large amount of AE during this experiment (more than 200,000), the *DaxBox* memory was overloaded when the effective pressure reached 140 MPa, and we were not able to record the AE events during an interval of pressure increasing from 140 to 145 MPa (Fig. 4a).

The sample deformed at an effective confining pressure of 10 MPa is representative of the brittle faulting regime (Figs. 3b, 4b). For reference, the hydrostatic loading is plotted as the dashed line (Fig. 3b). The differential stress attains a peak, beyond which strain softening is observed (Fig. 4b). The porosity initially decreases, but at a stress state C' it reverses to an increase indicating dilatation of the pore space (Fig. 3b). The AE data in this experiment follow a trend that has been reported in earlier studies (WONG *et al.*, 1997; ZANG *et al.*, 1998; LEI *et al.*, 2004; SCHUBNEL *et al.*, 2007): the critical stress state C' is associated with a surge in AE events (Fig. 4b) and the rupture is characterized by a surge in AE rate at an axial strain of $\sim 1\%$ (Fig. 4d). However the number of AE recorded during this experiment is only 10,000; one order of magnitude less than the AE number recorded during the experiment VO#5.

For the sample deformed at an effective confining pressure of 70 MPa, the failure mode is associated with an appreciable porosity reduction (Fig. 3c). In the first part of the loading, the triaxial data (solid curve) coincides with the hydrostat (dashed curve). However at stresses higher than C^* the deviatoric stresses contribute significantly to the compactive strain (Fig. 3c). This phenomenon of inelastic yield by “shear-enhanced compaction” (WONG *et al.*, 1997) is attributed to the inception of grain crushing and pore collapse in the sandstone (MENÉNDEZ *et al.*, 1996). During this second stage, strain hardening is observed (Fig. 4c). The number of AE events during this loading is given in

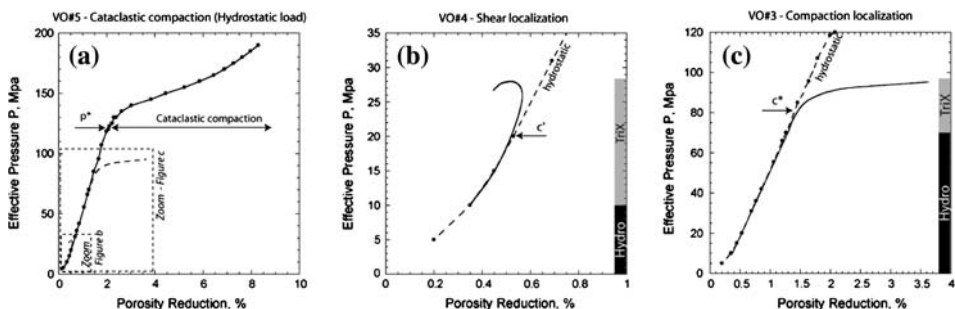


Figure 3

Effective mean pressure versus porosity reduction. a) Hydrostatic loading (for reference, the two triaxial experiments are shown as the dashed lines). b) and c) Triaxial compression experiments performed at effective confining pressure of 10 MPa and 70 MPa, respectively (for reference, the hydrostatic loading is shown as the dashed line). The critical stress state P^* , C' and C^* are indicated by arrows.

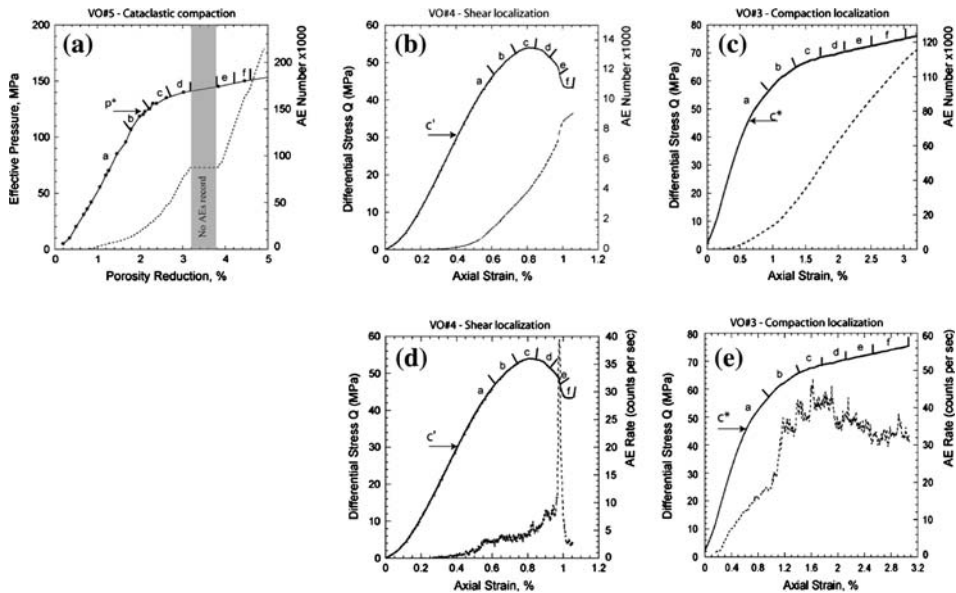


Figure 4

a) Hydrostatic experiment: Effective pressure (solid curve) and cumulative AE (dotted line) as functions of porosity reduction. Triaxial experiments: b) and c) differential stress (solid curve) and accumulative AE (dotted line) versus axial strain; d) and e) differential stress (solid curve) and AE rate (dotted line) versus axial strain. Effective confining pressure was 10 MPa in Figures b) and d) and 70 MPa in Figures c) and e). Six intervals are defined for each experiment (a to f) corresponding to the AE hypocenter distributions shown in Figure 5. The critical stress state P^* , C' and C^* are indicated by arrows.

Figure 4c. The critical stress state C^* is also associated with a surge in AE events as reported in WONG *et al.* (1997), WU *et al.* (2000), and BAUD *et al.* (2006). Cumulative AE events increase with strain, due to the progressive increase of damage (Fig. 4c). As pointed out by BAUD *et al.* (2004) important data to track compaction band is the AE rate. BAUD *et al.* (2004) and more recently STANCHITS *et al.* (this issue) correlated AE rate surges with the formation of discrete compaction bands. In our experiment AE rate surges can be observed (Fig. 4e). These surges are not as clear as those observed in experiments on Bentheim sandstone (BAUD *et al.* 2004; STANCHITS *et al.*, this issue), but can be compared to the observations from experiments on Diemelstadt sandstone (BAUD *et al.*, 2004). At an axial strain of 3.16% the number of AE events is $\sim 118,000$; a number comparable to the AE records performed during the experiment VO#5.

3.2. Acoustic Emissions Hypocenters

The three modes of failure are very different on the macroscopic scale, nonetheless they involve the same micromechanical processes (microcracking at grain scale; see Section 3.4). As a consequence these three modes of deformation lead to radiation of acoustic emissions.

Cataclastic compaction. AE locations from sample deformed under hydrostatic loading are shown in Figure 5 (top) and can be compared to the stress-strain curve plotted in Figure 4a. Stress increments *a-f* in Figure 4a correspond to the AE hypocenter distributions *a-f* shown in Figure 5 (top). Each dot represents one acoustic event. Whereas the loading is isotropic, the location of the AE indicates that the processes of grain crushing and pore collapse are not distributed homogeneously. In stage *a* of Figure 5 (top), the AE location shows that the events are mostly concentrated near the ends of the specimen. This is expected as stress concentrations due to end effects are important. However, in stage *b* AE events form clusters distributed through the specimen volume and AE concentrations near the ends due to end effects tend to disappear. The clusters formed in stage *b* grow during stages *c* and *d* and form compacted zones mostly distributed in the middle part of the specimen. In latest stages *e* and *f*, the compaction seems to be more homogeneous.

Shear localization. AE hypocenter locations registered during deformation of sample VO#4 in the brittle regime are given in Figure 5 (middle) and can be compared to the stress-strain curve plotted in Figure 4b. In stage *a*, AE activity appears near the ends of the sample as initial loading begins, probably due to end cap friction. During stages *b* and *c* around 3000 AE events are located and demonstrate the early stages of shear localization in the upper part of the specimen. During stage *d*, the stress starts to drop, and the nucleation zone prior to failure extends. Within the next stages *e* and *f*, unstable failure propagates through the upper part of the sample.

The AE hypocenter locations show that the failure propagates in the last stages of the loading (stages *e* and *f*). This result is consistent with the previous experiments on sandstone performed at AE rate control by LOCKNER *et al.* (1992). The initiation of shear localization appears, in stages *c* and *d*, in the upper left of the specimen. The initiation might have been controlled by some pre-existing heterogeneities, as seen by LEI *et al.* (2004) in granite or SCHUBNEL *et al.* (2007) in sandstone.

Compaction localization. AE locations registered during deformation of sample VO#3 at an effective confining pressure of 70 MPa are shown in Figure 5 (bottom) and can be compared to the stress-strain curve plotted in Figure 4c. Stress increments *a-f* in Figure 4c correspond to the AE hypocenter distributions *a-f* given in Figure 5 (bottom). In the first stage of the loading, the spatial distribution of the AE is similar to the location obtained during the first stage in VO#5 (the specimen deformed under hydrostatic loading): Events are located at the ends of the specimen and at the same time AE clusters form through the specimen volume. However, in this experiment, the migration of AE clusters is not random: In stage *b* the clusters propagate mostly normal to the compression direction. In stages *c* to *f* several discrete compaction bands formed normal to the compression direction can be observed. The overall AE activity is also more intense: 13 times more events were recorded during compaction localization than during shear localization. Two reasons explain such behavior in the overall AE activity: i) For the sample deformed by shear localization, rupture appears at an axial strain of $\sim 1\%$

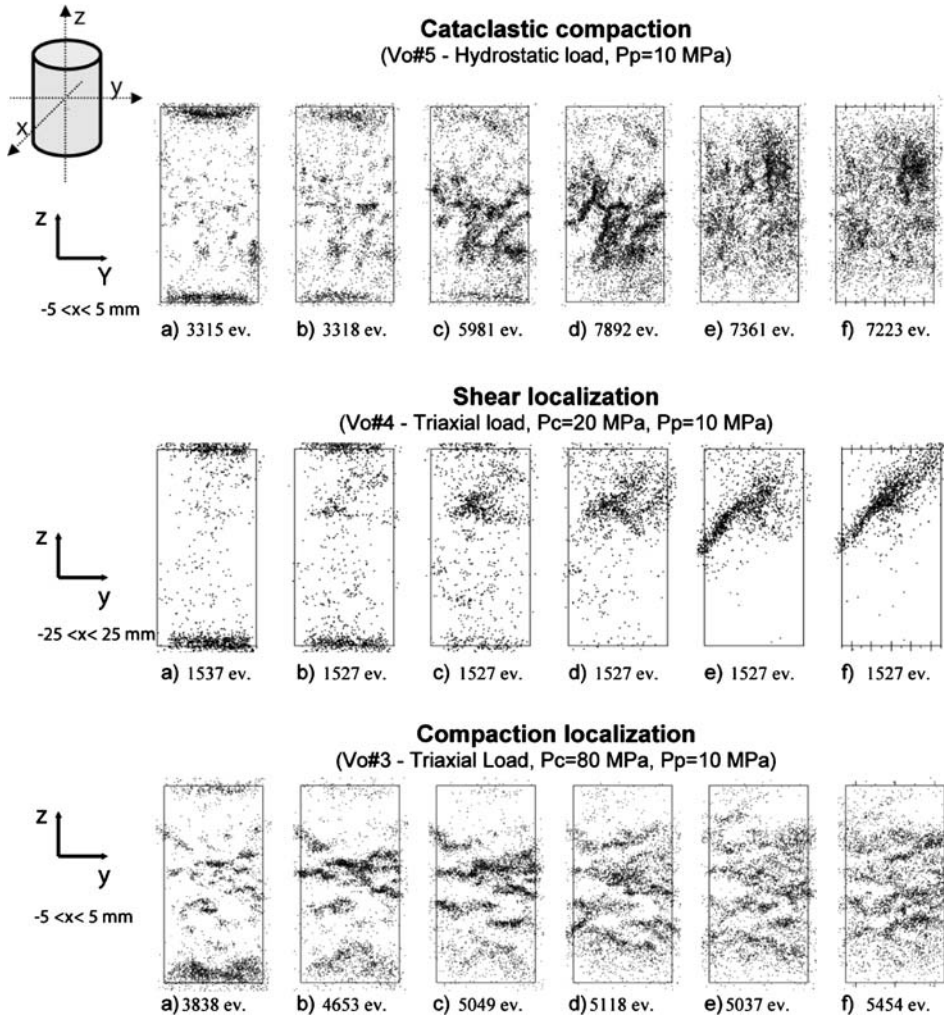


Figure 5

AE hypocenter distribution. The intervals (a to f) are defined in Figure 4. Top plot is a projection of all the events located between $-5 \text{ mm} < x < 5 \text{ mm}$, on the (z, y) plane recorded during the hydrostatic experiment. Middle plot is a projection of all the events on the (z, y) plane recorded during the triaxial experiment at 10 MPa effective confining pressure. Bottom plot is a projection of all the events located between $-5 \text{ mm} < x < 5 \text{ mm}$, on the (z,y) plane recorded during the triaxial experiment at 70 MPa effective confining pressure.

(Fig. 4d), however for the sample deformed by compaction localization, no rupture of the sample is observed and damage increases with progressive loading, ii) moreover, the damage volume induced by shear localization is less in comparison to the damage volume induced by compaction localization (Fig. 5).

In a recent study, TOWNEND *et al.* (2008) used AE to track the spatial and temporal evolution of a single, discrete, compaction band across the full diameter of a core sample

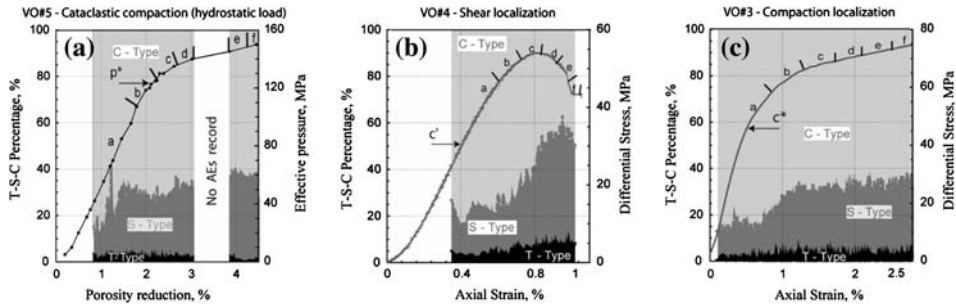


Figure 6

Top: Color code indicates AE-source type distribution during loading. C-, S-, and T-type events possibly represent signals radiated from pore collapse, shear and tensile cracks, respectively. The percentages of each part are indicated on the left vertical scale in the three figures: For example in Figure a) T-type, S-type, and C-type represent, respectively, $\sim 5\%$, $\sim 28\%$ and $\sim 67\%$ of the source mechanism. For reference, the evolution of effective pressure (right vertical scale) is plotted versus porosity reduction in Figure a). The evolution of differential stress versus axial strain (right vertical scale) is plotted in Figures b) and c).

of Diemelstadt sandstone. In contrast to our observations, TOWNEND *et al.* (2008) observed that compaction band growth in Diemelstadt sandstone originated at the sample boundary before propagating across the sample. Similar observations are also reported in STANCHITS *et al.* (this issue), from experiments done on notched samples. The nucleation of compaction band will be discussed in Section 4.1.

3.3. AE Source Characteristics

During the experiments, the full-waveform AE data are recorded which allows us to conduct *P*-wave first-motion studies (see ZANG *et al.*, 1996; LEI *et al.*, 1992; STANCHITS *et al.*, 2001). In our experiment local AE source mechanisms were separated into pure tensile mechanisms (T), shear-type events (S) and implosion type events (C) representing tensile cracks, shear cracks and pore collapse, respectively.

The results are summarized in Figure 6a for the specimen deformed under a hydrostatic loading, in Figure 6b for the specimen deformed in the brittle regime, and in Figure 6c for the specimen deformed at an effective confining pressure of 70 MPa. In the three experiments, the source type distribution reveals i) a dominance of pore collapse (C-type), ii) a small number of tensile cracks (T-type). During cataclastic compaction, S-type and C-type represent, respectively, $\sim 28\%$ and $\sim 67\%$ of the source mechanisms. For the specimen deformed in the brittle regime, the amount of shear-type events (S-type) increases from $\sim 20\%$ at the beginning of the loading to $\sim 50\%$ of all the events in the postfailure region where the sample strength drops. At the same time, the amount of pore collapse events decreases from $\sim 80\%$ to $\sim 40\%$. For the experiment performed at 70 MPa effective confining pressure, the amount of shear-type events increases from

~12% to ~26% during shear-enhanced compaction whereas the amount of pore collapse events decreases from ~84 % to ~70%.

The distribution of the events during cataclastic compaction and during the formation of compaction bands seems to be similar, indicating that the micromechanisms are similar. However, the development of a shear band is associated with a different acoustic signature. These results will be discussed in Section 4.2.

3.4. Microstructural Observation

Detailed microstructural analysis was performed on the three deformed specimens using scanning electron microscopy (SEM). To prepare SEM sections, samples 25×40 mm in size were cut parallel to the long specimen axis. Sections were impregnated with epoxy and subsequently polished and gold coated.

Cataclastic compaction. Figures 7a are SEM micrographs of the deformed sample and illustrate the extensive grain crushing that took place during deformation (compare Fig. 7a and Fig. 1b). The spatial distribution of damage is quite homogeneously in agreement with the last stages of the AE locations (Fig. 5, top). Grain fragments fill up the existing pores leading to a large decrease in porosity. The grain crushing process was probably triggered by extensile cracking initiated at the contact region where stress concentration had been induced by grain-grain contacts, in a manner analogous to the Hertzian fracture model proposed by ZHANG *et al.* (1990).

Shear localization. Figure 7b illustrates the damage evolution in the specimen that failed by dilatant failure and shear localization. The shear localization developed in the upper part of the sample along a planar zone, which is inclined at an angle of $\sim 45^\circ$ to σ_1 (Fig. 5, center and Fig. 7b). The width of the shear band is ~ 0.3 mm, which is ~ 3 times the average of mean grain diameter (0.11 mm). The central part of the localization shows an intense grain crushing. Inside the band, mica minerals accommodate the deformation, indicating displacement of neighboring quartz or feldspar grains. Outside the band, damage is very small. These observations are in agreement with those reported by MENÉNDEZ *et al.* (1996) in Berea sandstone and by BÉSUELLE *et al.* (2003) in Rothbach sandstone.

Compaction localization. In Figures 7c we present SEM micrographs corresponding to the specimen deformed at 70 MPa effective confining pressure. In these pictures, a compaction band appears as a zone of intensive cracking. The orientation of this zone is subhorizontal (perpendicular to σ_1), in agreement with the AE locations (Fig. 5, bottom). Grain crushing is evident; the fragments fill the pore space leading to a decrease in the overall porosity. The thickness is about ~ 0.6 mm which represents ~ 5 mean grain diameters. A compaction band in Bleurswiller sandstone appears thicker than those observed in Diemelstadt sandstone or Bentheim sandstone, where the thickness of a

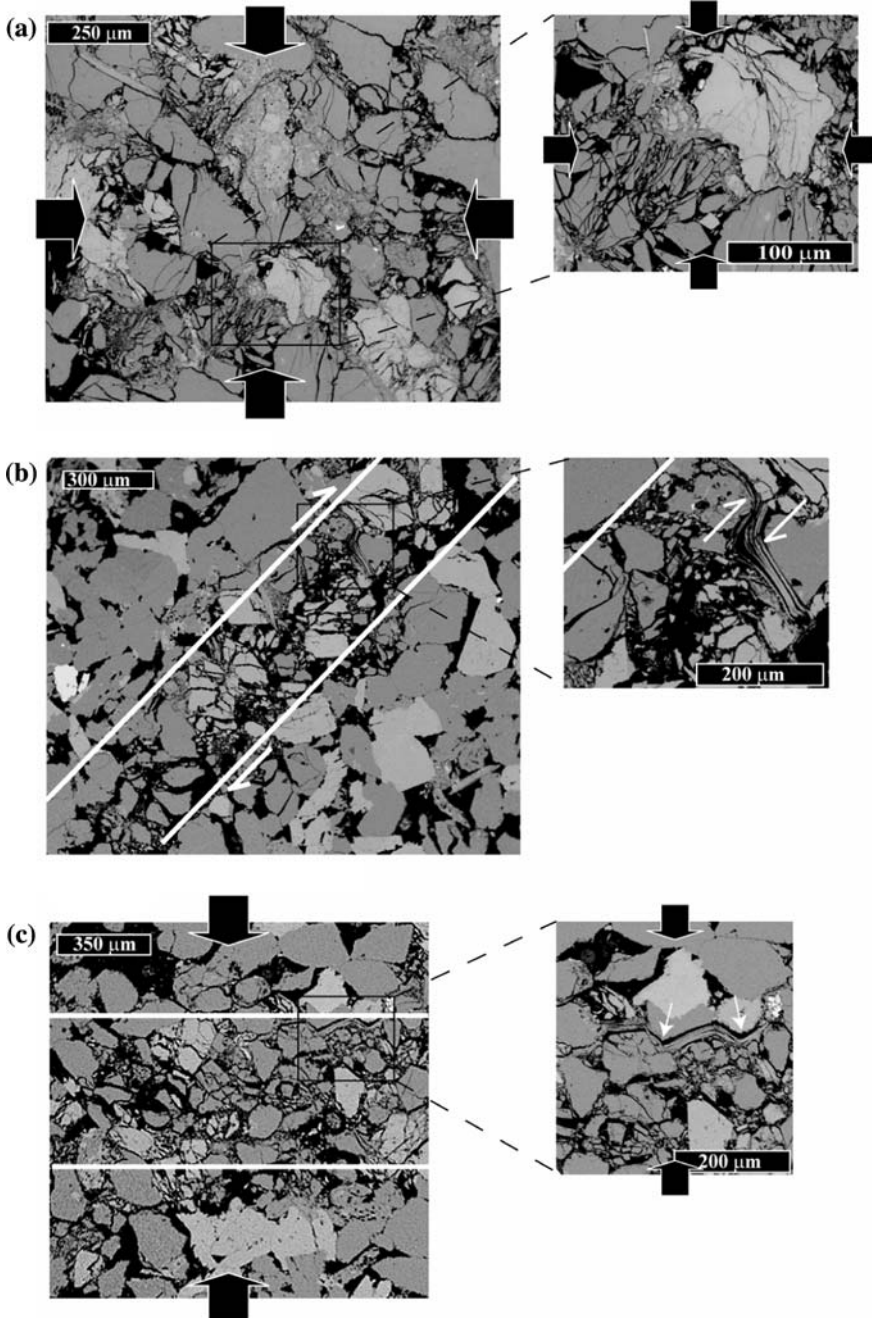




Figure 7

SEM micrographs (backscattered) of deformed Bleurswiller sandstone loaded a) under hydrostatic pressure (cataclastic compaction), b) in triaxial compression at an effective confining pressure of 10 MPa (Shear localization), c) in triaxial compression at an effective pressure of 70 MPa (compaction band). For b) and c) maximum compressive stress is vertical. Epoxy-filled pores appear in black. Grain crushing is pervasive in the three deformed specimens, which led to radiation of acoustic emissions.

compaction band represents $\sim 2\text{--}3$ grains (TEMBE *et al.*, 2008). Outside the band, the microstructure of the rocks remains largely undeformed with a porosity of $\sim 25\%$. Mica minerals are present, and accommodate the deformation, showing the displacement of neighboring quartz or feldspar grains.

4. Discussion

4.1. Nucleation and Propagation of Damaged Zones

From Figure 5, we observed that AE events occur during the early stages of loading in the three experiments. Following LOCKNER (1992), ZANG *et al.* (1998) and LEI *et al.* (2000) the behavior of the AE during the early stages is interpreted as indicating the presence of significant weak zones or zones of stress concentration which acted as nucleation sites. This interpretation is also confirmed by medical X-ray scanner tomography done by FORTIN *et al.* (2005) on an intact specimen: This technique reveals zones of several mm^2 of high porosity, randomly located in the sample. Using X-ray CT scan, a more precise technique, LOUIS *et al.* (2006) report in Rothbach sandstone, porosity variation reaching 7% across the sample. Pre-existing microcracks and high porosity regions appear to be the most important factors controlling the local strength of the rock, and thus controlling the nucleation sites.

For the specimen deformed at an effective confining pressure of 10 MPa (Fig. 5, center), the early AE events are relatively diffuse, however in stage *c*, local heterogeneity appears to be sufficient in magnitude to determine where failure will initiate.

For the specimen deformed at an effective confining pressure of 70 MPa, the early AE events form clusters (stages *a* and *b* in Figure 5, bottom). Local high porosity regions may determine the location of these clusters. Subsequently, these heterogeneities act as zones of stress concentration and initiate compaction bands. This process is similar to the effect of a notch, which induces stress concentration and facilitates the initiation of a compaction band (see STANCHITS *et al.*, this issue). In notched specimens only one compaction band is initiated. In contrast, in Bleurswiller sandstone, local heterogeneities can induce several bands. However, in our specimen, when compaction bands propagate, they can merge (stages *c* and *d* on Figure 5, bottom). As a consequence, compaction bands in Bleurswiller sandstone are not perfectly plane, but are an association of parts of pure compaction localization formed perpendicular to the main compressive axis connected with small shear bands.

For the specimen deformed under hydrostatic loading, the local heterogeneities appear to be sufficient to induce AE clusters (stage *b* on Figure 5, top). However, in this experiment the orientation of the compacted zones seems to be random (stages *c* and *d* on Figure 5, bottom). With increasing pressure, the compacted zones merge, and in the last stages the AE event distribution seems to be more diffuse. Local heterogeneities may control the early stages of the deformation during the formation of compaction bands and during cataclastic compaction. To understand further the role of local heterogeneities in the process of Bleurswiller sandstone deformation, it would be useful to perform X-ray CT scan (where the resolution is in the order of $\sim 50 \mu\text{m}$), because with this nondestructive method it would be possible to acquire images of the same sample before and after failure (LOUIS *et al.*, 2006).

4.2. Micromechanics of Failure

The ratio of shear-type cracking (S-type) to pore collapse event (C-type) is related to the stress boundary conditions and porosity of the sample. Tensile cracking appears to be negligible. The ratio $\frac{\text{S-type}}{\text{C-type}}$ during cataclastic compaction is ~ 0.41 ; a similar ratio of ~ 0.37 is obtained during formation of compaction bands (Fig. 6). During the formation of shear localization the ratio increases to ~ 1.25 . Thus during the three experiments, AE source types indicate dominance of pore collapse and shear cracking. However, shear cracks are seldom seen in the microstructure (Fig. 7). What causes this source type distribution?

First, it is important to keep in mind that the AE records represent a small fraction of the total damage. For example, during the deformation of the specimen under hydrostatic loading, about 220,000 AE events were typically detected. For a grain size of $\sim 110 \mu\text{m}$, this gives approximately one AE event for every $\sim 1,000$ grains, or a mean distance $\langle l \rangle$ between two AE locations of $\langle l \rangle \approx 10 d$, where d is the mean grain diameter. During experiment VO#4, where shear localization was observed, around 9,000 AE events were recorded. Assuming that the damage volume could be roughly estimated as the area of the shear localization (27.9 cm^2) multiplied by the thickness of the band (0.3 mm), this gives approximately one AE event for every ~ 150 grains or a mean distance $\langle l \rangle$ between two AE locations of $\langle l \rangle \approx 5 d$, similar to the result found in the hydrostatic experiment. In his paper LOCKNER *et al.* (1992) recorded, using a different threshold level, $\sim 5,000$ AE events during shear localization in sandstone, which is approximately one event for every $\sim 3,000$ grains. Thus cracking events detected by AE represent a small fraction of the total microcrack damage occurring in the rock. However, the excellent agreement between AE locations and observed fault or compaction bands found by LOCKNER and BYERLEE (1977), LEI *et al.* (2004), FORTIN *et al.* (2006) and STANCHITS *et al.* (this issue) support the idea that microcracks detected by AE are representative of the overall microcrack population.

Figure 8 gives a conceptual model of a tensile event (Fig. 8a), a shear type event (8b) and a pore collapse event (8c). A pore collapse event is a mixed mode: a pore collapse event is a consequence of re-arrangement of the grain-packing (Fig. 8d). In order to collapse the pore, grains and parts of the cement need to be broken (8c, 8d); the breakage

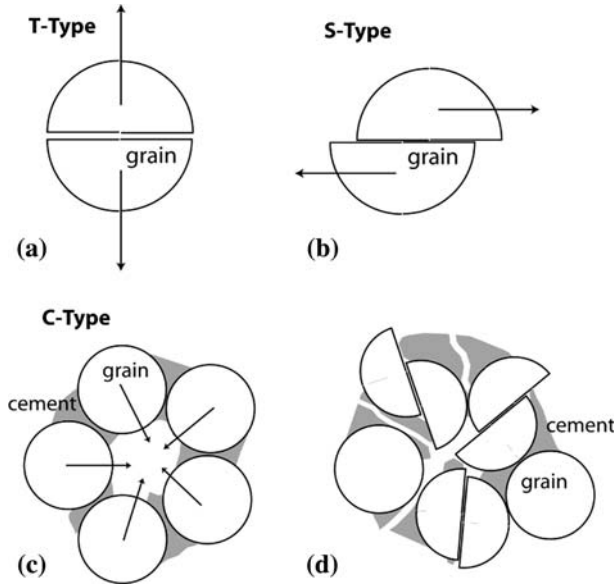


Figure 8

Conceptual model of a tensile event (a), a shear-type event (b) and a pore collapse event (c). A pore collapse event is a mixed mode: a pore collapse event is a consequence of a packed re-arrangement (d). Note that breakage of some grains or/and cement is needed to collapse a pore and radiate a C-type event.

of grains and then the collapse of the pore lead to a collapse event (C-type) (STANCHITS *et al.*, 2001).

During the formation of shear localization (Fig. 6b) our AE source type analysis indicates a ratio of shear-type cracking to pore collapse events of ~ 1.25 , in agreement with the study of ZANG *et al.* (2000). However, during the formation of compaction bands and cataclastic compaction our AE focal analysis indicates a ratio of ~ 0.4 . From Figure 8c, we would expect that these two kinds of inelastic deformation would be associated with pore collapse events and shear-type sources (see above). Two explanations can be given: i) Pore collapse induced grain cracking (Fig. 8d), thus with loading these cracks can be activated (frictional shearing) and radiate shear-type events; ii) from AE locations, we suggested in Section 4.2 that the interaction between two compaction bands can lead to small shear bands when they merge. Thus, these small shear bands can also lead to shear-type events.

4.3. Yield Surface

Data for the brittle strength and compressive yield stress are compiled in Figure 9. The equivalent von Mises shear stress for a compressive axisymmetric stress state are defined by $\tau = (\sigma_1 - \sigma_3)/\sqrt{3} = Q/\sqrt{3}$. The stress path of the three experiments presented in this study (VO#3; VO#4, VO#5) are drawn as grey dashed-lines. Data of FORTIN *et al.*

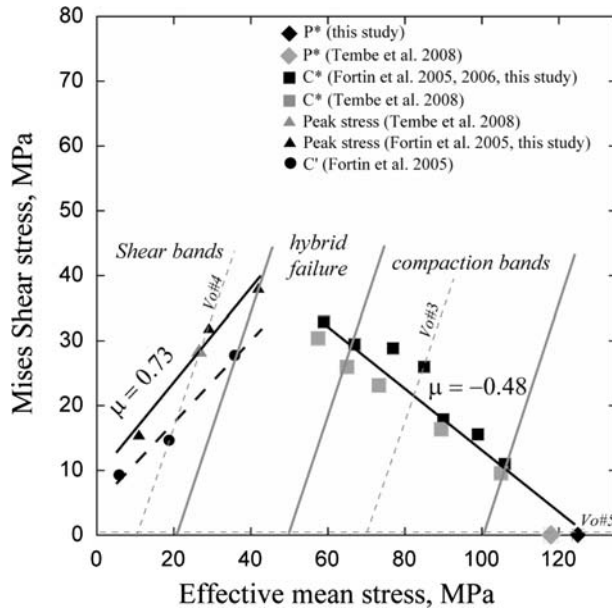


Figure 9

Peak stress, onset of dilatancy (stress state C') and onset of shear-enhanced compaction (C*) in the Von Mises shear stress versus effective mean stress plane. Note that elastic domain can be delimited by two straight lines. μ can be inferred from the slope of the lines and denotes the friction coefficient.

(2005, 2006, 2007) and TEMBE *et al.* (2008) are also included. Duplicate experiments indicate that experiments performed on cylindrical specimens of 38.1 mm in length and 18.4 mm in diameter (grey symbols on Fig. 9, TEMBE *et al.*, 2008) lead to peak stresses and compactive yield stresses lower than the values inferred from experiments performed on bigger specimens (black symbols): in FORTIN *et al.* (2005) and (2007) the length and diameter of the specimens are 80 mm and 40 mm, respectively; and in this study and in FORTIN *et al.* (2006) the length and diameter of the specimens are 100 mm and 50 mm, respectively.

The shape of the yield envelope controls the predictions of bifurcation analyses (RUDNICKI and RICE, 1975; ISSEN and RUDNICKI, 2000; BÉSUELLE, 2001, RUDNICKI, 2004). One of the important parameter is the pressure-sensitivity parameter μ , which can be inferred from the slope of the yield stress data as indicated in Figure 9. In the brittle regime the elastic domain can be bounded by a line, with a positive slope $\mu = 0.73$. This value is inferred from all the data plotted on Figure 9. In the compactive regime, yield stresses (C*) usually map an ellipse (WONG *et al.*, 1997; BAUD *et al.*, 2006), however our data show that compactive yield stresses in Bleurswiller sandstone rather map a straight line, with a negative slope $\mu = -0.48$, a value inferred from all the data plotted on Figure 9. The physical explanation for the geometry of the yield envelope in the

compactive domain remains unclear: It can be due to the presence of heterogeneity in the rock; it can also be the consequence of a nonnegligible part of mica minerals in the mineralogical composition of the rock.

5. Conclusions

In this paper, three modes of deformation were investigated during the compaction of porous rock. Under hydrostatic pressure, a large mechanical decrease of porosity is observed at a critical pressure, where pore collapse and grain crushing occur. Under axisymmetric compression, the mechanical response of the sample deformed at 10 MPa effective confining pressure is characterized by brittle faulting. However, at 70 MPa effective confining pressure, compaction bands can be observed.

From acoustic emission records, we observed that;

- i) The number of acoustic events during shear localization is around one order of magnitude less than the number of events recorded during the formation of compaction bands or during cataclastic compaction. However, the mean distance between two AE locations is, in both experiments, in the same range (between 5 and 10 d , where d is the mean grain diameter). In fact, the occurrence of AE activity is associated with the total damage volume, which is more important during cataclastic compaction or during the formation of compaction bands than during shear localization.
- ii) AE locations allow us to characterize the spatial evolution of the damage in the rock during the three modes of deformation. Nucleation seems to be strongly affected by material heterogeneity (high local porosity). The AE locations indicate that the early stages of deformation during the formation of compaction bands and during cataclastic compaction are similar.
- iii) First-motion studies show that the micromechanisms taking place during the formation of compaction bands and cataclastic compaction are similar (predominance of pore collapse events), whereas the shear localization is characterized by a different acoustic emission signature (predominance of shear events).

Acknowledgments

We are grateful to Patrick Baud and the anonymous reviewer for their careful and critical comments. The authors would particularly like to thank Stefan Gehrmann (GeoForschungsZentrum, Potsdam) for aid in preparing the thin sections, and Nathanael Findling (Ecole normale supérieure, Paris) for aid in SEM analysis. This work was partially supported by the French-German grant "Procope".

REFERENCES

- BAUD, P., KLEIN, E., and WONG, T.-F. (2004), *Compaction localization in porous sandstones: Spatial evolution of damage and acoustic emission activity*, J. Struct. Geol. 26, 603–624.
- BAUD, P., VAJDOVA, V., and WONG, T.-F. (2006), *Shear-enhanced compaction and strain localization: Inelastic deformation and constitutive modeling of four porous sandstones*, J. Geophys. Res. 111, B12401, doi:[10.1029/2005JB004101](https://doi.org/10.1029/2005JB004101).
- BÉSUELLE, P. (2001), *Compacting and dilating shear bands in porous rocks: Theoretical and experimental conditions*, J. Geophys. Res. 106, 13435–13442.
- BÉSUELLE, P., BAUD, P., and WONG, T.-F. (2003), *Failure mode and spatial distribution of damage in Rothbach sandstone in the brittle-ductile transition*, Pure Appl. Geophys. 160, 851–868.
- DAVID, C., WONG, T.-F., ZHU, W., and ZHANG, J. (1994), *Laboratory measurement of compaction induced permeability change in porous rocks: Implication for the generation and maintenance of pore pressure excess in the crust*, Pure Appl. Geophys. 143, 425–456.
- FORTIN, J., GUÉGUEN, Y., and SCHUBNEL, A. (2007), *Effect of pore collapse and grain crushing on ultrasonic velocities and V_p/V_s* , J. Geophys. Res. 112, doi:[10.1029/2005JB004005](https://doi.org/10.1029/2005JB004005).
- FORTIN, J., STANCHITS, S., DRESEN, G., and GUÉGUEN, Y. (2006), *Acoustic emission and velocities associated with the formation of compaction bands*, J. Geophys. Res. 111, B10203, doi:[10.1029/2005JB003854](https://doi.org/10.1029/2005JB003854).
- FORTIN, J., SCHUBNEL, A., and GUÉGUEN, Y. (2005), *Elastic wave velocities and permeability evolution during compaction of Bleurswiller sandstone*, Int. J. Rock Mech. Min. Sci. Geomech. 42, 2005, 873–889.
- GRUESCHOW, E. (2005a), *Yield cap constitutive models for predicting compaction localization in high porosity sandstone*, Ph.D. Thesis, Northwestern Univ., Evanston, Ill.
- GRUESCHOW, E. and RUDNICKI, J. W. (2005b), *Elliptic yield cap constitutive modeling for high porosity sandstone*, Int. J. Solids Struct. 42, 4574–4587.
- ISSEN, K. A. and RUDNICKI, R. J. (2000), *Conditions for compaction bands in porous rock*, J. Geophys. Res. 105, 21529–21536.
- KLEIN, E., BAUD, P., REUSCHLE, T., and WONG, T.-F. (2001), *Mechanical behavior and failure mode of Bentheim sandstone under triaxial compression*, Phys. Chem. Earth, Part A 26, 21–25.
- LEI, X., NISHIZAWA, O., KOSE, K., and SATOH, T. (1992), *Fractal structure of the hypocenter distributions and focal mechanism solutions of acoustic emission in two granites of different grain sizes*, J. Phys. Earth. 40, 617–634.
- LEI, X., NISHIZAWA, O., KUSUNOSE, K., CHO, A., and SATOH, T. (2000), *On the compressive failure of shale samples containing quartz-healed joints using rapid AE monitoring: the role of asperities*, Tectonophysics 328, 329–340.
- LEI, X.-L., MASUDA, K., NISHIZAWA, O., JOURNIAUX, L., LIU, L., MA, W., SATOH, T., and KUSUNOSE, K. (2004), *Detailed analysis of acoustic emission activity during catastrophic fracture of faults in rock*, J. Struct. Geol. 26, 247–258.
- LOCKNER, D. A. and BYERLEE, J. D., *Acoustic emission and fault formation in rocks*, In *Proc 1st Conf. on Acoustic Emission/Microseismic Activity in Geol. Structures and Materials* (eds. H.R., Hardy and F.W., Leighton), (Trans-Tech. Publications, Clausthal-Zellerfeld 1977), pp. 99–107.
- LOCKNER, D. A. (1993), *The role of acoustic emission in the study of rock fracture*, Int. J. Rock Mech. Min. Sci. Geomech. 30, 883–899.
- LOCKNER, D.A., BYERLEE, J. D., KUKSENKO, V., PONOMAREV, A., and SIDORIN, A., *Observation of quasistatic fault growth from acoustic emissions*. In *Fault Mechanics and Transport Properties of Rocks* (eds. B. Evans and T.-f. Wong), (Academic Press 1992) pp. 3–31.
- LOUIS, L., WONG, T-F, BAUD, P., and TEMBE, S. (2006), *Imaging strain localization by X-ray computed tomography: Discrete compaction bands in Diemelstadt sandstone*, J. Struct. Geol. 28, 5, 762–775.
- MÉNENDEZ, B., ZHU, W., and WONG, T.-F. (1996), *Micromechanics of brittle faulting and cataclastic flow in Berea sandstone*, J. Struct. Geol. 18, 1–16.
- NAGEL, N. B. (2001), *Compaction and subsidence issues within the petroleum industry: From Wilmington to Ekofisk and beyond*, Phys. Chem. Earth 26, 3–14.
- OLSSON, W. A. and HOLCOMB, D. J. (2000), *Compaction localization in porous rock*, Geophys. Res. Lett. 27, 3537–3540.
- OSTERMEIER, R. M. (2001), *Compaction effects on porosity and permeability: Deepwater Gulf of Mexico turbidites*, J. Pet. Technol. 68–74.

- RUDNICKI, J. W. and RICE, J. R. (1975), *Conditions for the localization of deformation in pressure sensitive dilatant materials*, J. Mech. Phys. Solids 23, 371–394.
- RUDNICKI, J. W. (2004), *Shear and compaction band formation on an elliptic yield cap*, J. Geophys. Res. 109, B03402, doi:[10.1029/2003JB002633](https://doi.org/10.1029/2003JB002633).
- SANO, O., ITO, I., and TERADA, M. (1981), *Influence of strain rate on dilatancy and strength of oshima granite under uniaxial compression*, J. Geophys. Res. 86 (B10), 9299–9311.
- SCHOLZ, C. H. (1968), *Microfracturing and the inelastic deformation of rock in compression*, J. of Geophys. Res. 73, 1471–1432.
- SCHUBNEL, A., THOMPSON, B., FORTIN, J., GUÉGUEN, Y., and YOUNG, R. P. (2007), *Pore pressure induced rupture and aftershocks on intact and fractured sandstone in the laboratory*, Geophys. Res. Lett. 34, doi:[10.1029/2007GL031076](https://doi.org/10.1029/2007GL031076).
- STANCHITS, S., ZANG, A., and DRESEN, G. (2001), *Focal mechanisms of acoustic emission events during fault propagation and friction sliding*, EOS Trans. AGU 82 (47), Fall Meet. Suppl., Abstract T51A-0847.
- STANCHITS, S., DRESEN, G., and VINCIGUERRA, S. (2006), *Ultrasonic velocities, acoustic emission characteristics and crack damage of basalt and granite*, Pure Applied Geophys. 163, 5–6, 975–994.
- STANCHITS, S., FORTIN, J., GUÉGUEN, Y., and DRESEN, G. (2009), *Initiation and propagation of compaction bands in dry and wet Benthem sandstone*, this issue.
- TEMBE, S., BAUD, P., and WONG, T.-F. (2008), *Stress conditions for the propagation of discrete compaction bands in porous sandstone*, accepted in J. Geophys. Res.
- TOWNEND, E., THOMPSON, B., BENSON, P. M., MEREDITH, P. G., BAUD, P., and YOUNG, R. P. (2008), *Imaging compaction band propagation in Diemelstadt sandstone using acoustic emission locations*, Geophys. Res. Lett. 35, L15301, doi:[10.1029/2008GL034723](https://doi.org/10.1029/2008GL034723).
- VAJDOVA, V., BAUD, P., and WONG, T.-F. (2004), *Permeability evolution during localized deformation in Benthem sandstone*, J. Geophys. Res. 109, B10406, doi:[10.1029/2003JB002942](https://doi.org/10.1029/2003JB002942).
- WU, X. Y., BAUD, P., and WONG, T.-F. (2000), *Micromechanics of compressive failure and spatial evolution of anisotropic damage in Darley Dale sandstone*, Int. J. Rock Mech. Min. Sci. 37, 143–160.
- WONG, T.-F., DAVID, C., and ZHU, W. (1997), *The transition from brittle faulting to cataclastic flow in porous sandstone: Mechanical deformation*, J. Geophys. Res. 102, 3009–3025.
- WONG, T.-F., DAVID, C., and MENÉNDEZ, B., *Mechanical compaction*. In *Mechanics of Fluid-Saturated Rocks*, Int. Geophys. Ser., vol. 89 (eds. Y., Guéguen and M., Bouteau), (Elsevier, New York 2004), pp. 55–114.
- ZANG, A., WAGNER, F. C., and DRESEN, G. (1996), *Acoustic emission, microstructure, and damage model of dry and wet sandstone stressed to failure*, J. Geophys. Res. 101, 17507–17521.
- ZANG, A., WAGNER, C. F., STANCHITS, S., DRESEN, G., ANDRESEN, R., and HAIDEKKER, M. A. (1998), *Source analysis of acoustic emissions in Aue granite cores under symmetric and asymmetric compressive loads*, Geophys. J. Int. 135, 1113–1130.
- ZANG, A., WAGNER, C. F., STANCHITS, S., JANSSEN, C., and DRESEN, G. (2000), *Fracture process zone in granite*, J. Geophys. Res. 105, 651–661.
- ZHANG, J., WONG, T.-F., and DAVIS, D. M. (1990), *Micromechanics of pressure-induced grain crushing in porous rocks*, J. Geophys. Res. 95, 341–352.

Received June 6, 2008, revised January 27, 2009, accepted February 13, 2009

Published Online First: May 12, 2009

To access this journal online:
www.birkhauser.ch/pageoph
